

An Unconventional Transient Phase with Cycloidal Order of Polarization in Energy-Storage Antiferroelectric PbZrO₃

Xian-Kui Wei,* Chun-Lin Jia, Hong-Chu Du, Krystian Roleder, Joachim Mayer, and Rafal E. Dunin-Borkowski

Antiferroelectric-based dielectric capacitors are receiving tremendous attention for their outstanding energy-storage performance and extraordinary flexibility in collecting pulsed powers. Nevertheless, the in situ atomic-scale structuralevolution pathway, inherently coupling to the energy storage process, has not been elucidated for the ultimate mechanistic understanding so far. Here, timeand atomic-resolution structural phase evolution in antiferroelectric PbZrO₃ during storage of energy from the electron-beam illumination is reported. By employing state-of-the-art negative-spherical-aberration imaging technique, the quantitative transmission electron microscopy study presented herein clarifies that the hierarchical evolution of polar oxygen octahedra associated with the unit-cell volume change and polarization rotation accounts for the stepwise antiferroelectric-to-ferroelectric phase transition. In particular, an unconventional ferroelectric category—the ferrodistortive phase characteristic of a unique cycloidal polarization order—is established during the dynamic structure investigation. Through clarifying the atomic-scale phase transformation pathway, findings of this work unveil a new territory to explore novel ferrodistortive phases in energy-storage materials with the nonpolar-to-polar phase transitions.

Benefit from the ultrafast charging/discharging rates, high voltage endurance, superior reliability and broad operating temperature, [1,2] dielectric-based electrostatic capacitors are becoming

Dr. X.-K. Wei, Prof. C.-L. Jia, Dr. H.-C. Du, Prof. J. Mayer,

Prof. R. E. Dunin-Borkowski

Ernst Ruska-Centre for Microscopy and Spectroscopy with Electrons

Research Centre Jülich Jülich 52425, Germany

E-mail: x.wei@fz-juelich.de

Prof. C.-L. Jia

School of Microelectronics

Xi'an Jiaotong University

Xi'an 710049, China

Dr. H.-C. Du, Prof. J. Mayer

Gemeinschaftslabor für Elektronenmikroskopie (GFE) RWTH Aachen

Ahornstraße 55, Aachen 52074, Germany

Prof. K. Roleder Institute of Physics University of Silesia Chorzów 41500. Poland



© 2020 The Authors. Published by WILEY-VCH Verlag GmbH & Co. KGaA, Weinheim. This is an open access article under the terms of the Creative Commons Attribution License, which permits use, distribution and reproduction in any medium, provided the original work is properly cited.

DOI: 10.1002/adma.201907208

critical components for many electrical power systems, e.g., portable/wearable electronics and collection of fluctuating energy sources. With adoption of different design strategies, e.g., polymorphic nanodomain,[3] chemical doping^[4] and structure sandwiching,[5] the recoverable energy density has been improved from ≈5 to over 150 J cm⁻³ in the past decade.^[5,6] Among the dielectrics, antiferroelectric-based capacitors serve as an important group of energy-storage materials, where the energy density stored through the antiferroelectric-ferroelectric (AFE-FE) phase transition can be expressed as $U_{e} = \int E \, dP$ with respect to the applied electric field E and the induced polarization P(Figure 1a).^[7] Nevertheless, with regard to the concrete structural evolution, [8,9] the ultimate mechanistic understanding has never been elucidated so far from experiments. This seriously hinders the development of new materials for energy storage and conversion.

Exploring the emergence of a net polarization from the nonpolar matrix plays a key role in understanding the energystorage process. Compared with other characterization techniques, in situ transmission electron microscopy (TEM) holds the promise of exposing the atomic-scale structural information. However, such a dynamic study is also challenged by a number of practical difficulties. i) A strong electric field is required to activate the phase transition, which is up to ≈220 kV cm⁻¹ for pure PbZrO3.[10] Being close to the strength of dielectric breakdown, the field may directly destroy the specimen. ii) It has been reported by in situ selected-area electron diffraction (SAED) and X-ray diffraction studies that the AFE-FE transition completes instantly at the critical switching field.[11-13] This implies that possible intermediate phases are simply concealed during the transition process. iii) Nucleation of the FE phase, reverse piezoelectric effect and domain reorientation^[14] under electric field set obstacles to acquire atomically resolved structural data. iv) To accurately analyze the structural change, tracking the evolution of intricate structural order parameters, e.g., the cationic displacement order and antiferrodistortive (AFD) oxygen octahedra, [9,15,16] poses a high demand on the detection technique and quality of the collected data.

As a prototypical energy-storage material, PbZrO₃ undergoes an AFE–paraelectric (PE) phase transition at $T_{\rm C}\approx 506~{\rm K},^{[17]}$ around which an FE rhomhohedral (FE_R) phase appears in a narrow ($\approx 20~{\rm K}$) temperature window. [18–20] With small

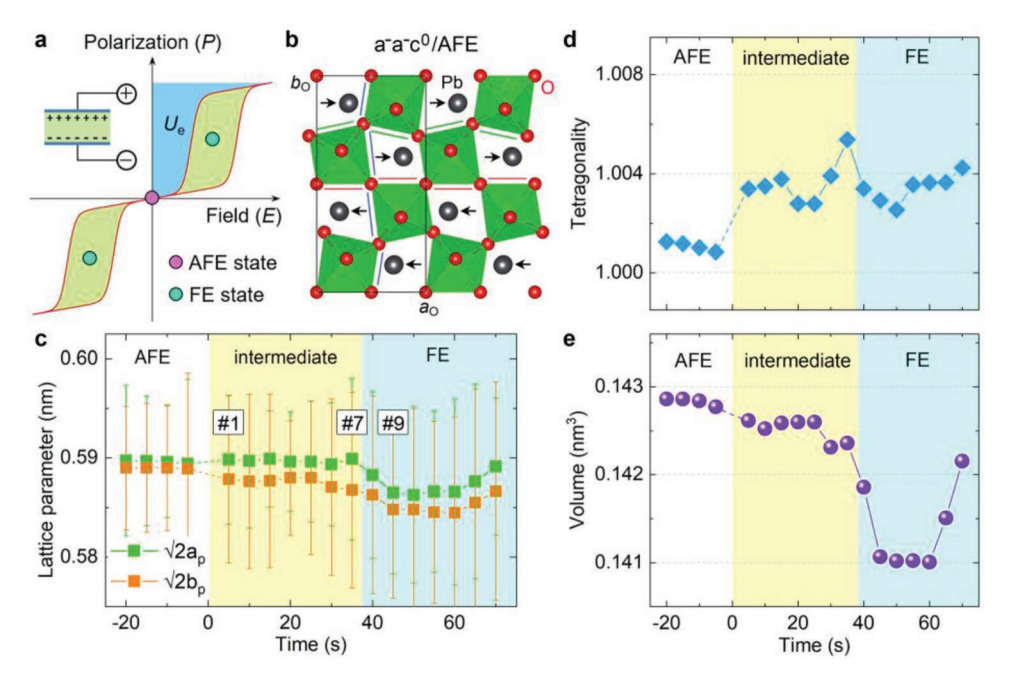


Figure 1. a) The double electrical hysteresis loop of typical AFEs along with the schematic capacitor geometry for energy storage. The blue area denotes the recoverable energy-storage density U_e . b) The antiparallel Pb shifts (black arrows) and AFD order induced buckling of oxygen chains (colorful solid lines) in AFE PbZrO₃ viewed along the [001]_O direction. c) Lattice parameter ($\sqrt{2}a_p$, $\sqrt{2}b_p$) evolution as a function of electron-beam irradiation time from a thin region of interest of PbZrO₃ viewed along the [001]_O//[001]_p direction. d,e) Evolution of lattice tetragonality ($\sqrt{2}a_p/\sqrt{2}b_p$) and volume ($V = \sqrt{2}a_p \times \sqrt{2}b_p \times c_p$) as a function of irradiation time, respectively.

amount of chemical doping, additional structural phases can be introduced into the phase diagram, e.g., AFE tetragonal phase in PbZr_{1-x}Ti_xO₃ (PZT, x=0.03) and (Pb_{1-y}Sr_y)ZrO₃ (0 < γ < 0.27). [21,22] The existence of FE monoclinic (FE_M) phases in the phase diagram of PZT (0 ≤ x ≤ 1) further complicates the phase constituents of PbZrO₃ near the transition temperature. [23–25] As $T_{\rm C}$ is approached from the PE side, the PbZrO₃ also exhibits complex structural features, e.g., an incipient FE state arising from competition of polar clusters with elastic anomalies, [26] and covalent bonding of disordered Pb with neighboring oxygen. [27,28] The complexity of structural polymorphs highlights the necessity of clarifying the phase-change route for understanding the energy-storage process.

Here, we employ the illumination electron beam, as an external driving force, [29–31] to consecutively excite and characterize the phase transitions of PbZrO3 crystal in an aberration-corrected TEM. By using the negative spherical-aberration imaging (NCSI) technique, [32,33] we simultaneously resolve the evolution of oxygen octahedra and cationic displacement order at seconds-level time and atomic resolution. Our simulation-based quantitative study reveals that the AFD–ferrodistortive (FD) transition of oxygen octahedra breaks the spatial inversion symmetry, and creates a novel cycloidal polarization order in the "AFE" orthorhombic lattice. Associated with successive volume change and polarization rotation, the FE–FD phase further transforms to a FE_M phase and then to the FE_R phase. Our time- and atomic-resolution TEM study provides a novel insight to understand the phase-transition pathway in PbZrO3-based energy-storage materials.

The AFE orthorhombic phase of PbZrO₃ has lattice parameters of $a_{\rm O} = \sqrt{2}a_{\rm p}$, $b_{\rm O} = 2\sqrt{2}a_{\rm p}$, and $c_{\rm O} = 2c_{\rm p}$ ($a_{\rm p}$, $b_{\rm p}$, and $c_{\rm p}$ are pseudocubic cell parameters).^[34] Apart from the

characteristic antiparallel Pb displacements in pairs along the $[100]_{\rm O}//[110]_{\rm p}$ direction, the AFD oxygen octahedra rotating along the $[210]_{\rm O}//[100]_{\rm p}$ and $[210]_{\rm O}//[010]_{\rm p}$ axes are manifested by buckling of oxygen chains along the $[100]_{\rm O}$ and $[010]_{\rm O}$ directions (Figure 1b). Using dark-field imaging, morphology of the AFE PbZrO $_{\rm 3}$ crystal is characterized and the inherent translation boundaries are clearly seen (Figure S1, Supporting Information). In our in situ experiments, a series of atomic-resolution images were recorded along the $[001]_{\rm O}//[001]_{\rm p}$ direction under the NCSI conditions.

By fitting and mapping the atom-column peak positions using a 2D Gaussian function (see the Experimental Section), we measured the lattice parameters from the atomic-resolution images and subtle lattice changes were identified during the phase transitions. Compared with the typical AFE phase, a_0 = 0.5896 nm and $b_0/2 = 0.5890$ nm (t < 0 s) (Figure 1c), a constant a_0 and a reduced $b_0/2$ by $\approx -0.22\%$ characterize an intermediate phase at t > 0 s. Continuous irradiation transforms the intermediate phase into a pseudocubic phase, where the lattice parameters are reduced to $\sqrt{2}a_p = 0.5865$ nm and $\sqrt{2}b_p =$ 0.5846 nm and then increased again. Accordingly, the lattice tetragonality defined as $T_L = \sqrt{2a_p/\sqrt{2}} b_p$ increases from 1.001 in the AFE phase to ≈1.003 in the intermediate and pseudocubic phases (Figure 1d). Meanwhile, the unit-cell volume, $V = \sqrt{2a_p} \times \sqrt{2} \ b_p \times c_p$ (constant $c_p = 0.4113$ nm), reduces from 0.1428 to 0.1410 nm3 via the intermediate phase and then increases to 0.142 nm3 (Figure 1e). The structural changes indicate that the phase transitions are of first orders.

From the intermediate phase zone (Figure 1c), our analysis on the displacement behavior of oxygen columns in image #1 reveals a particular region of interest, which is featured by a

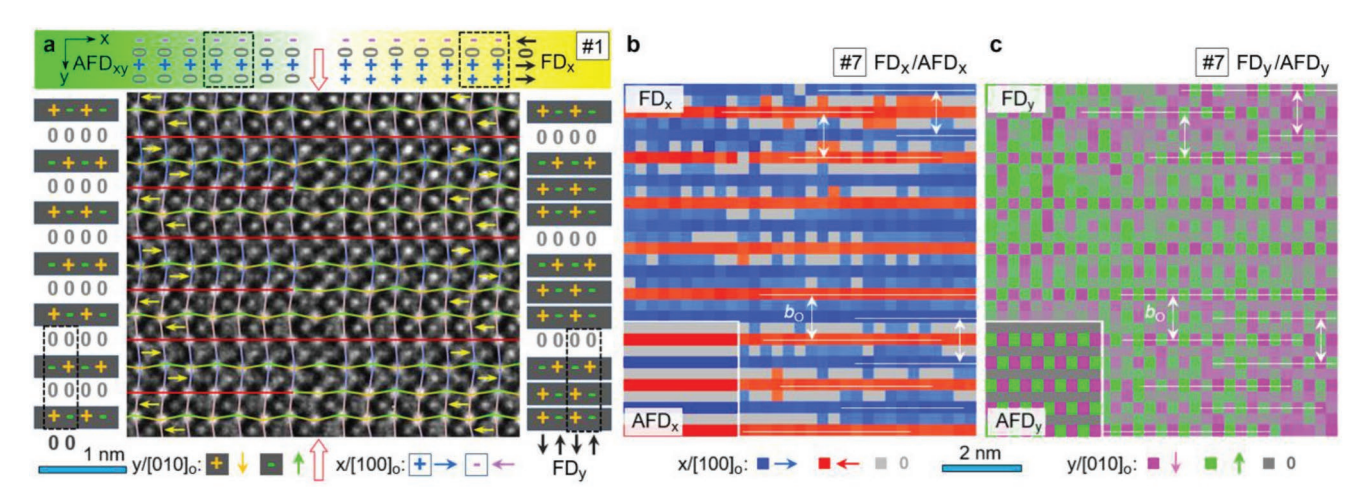


Figure 2. a) Atomic-resolution TEM image (#1) of AFD–FD phase boundary (empty red arrows) with annotation of antiparallel Pb displacements (yellow arrows). The oxygen displacement behaviors are indexed by (+, 0, -) signs at the edges and colorful solid lines on the image. The black arrows mark row (x)- or column (y)-based net displacements of oxygen in the AFE orthorhombic unit cell (black dashed rectangles). b,c) The FD_x and FD_y component maps measured from the atomic-resolution image (#7) of the intermediate phase (see Figure S1 in the Supporting Information) and compared with the AFD_x and AFD_y maps of the AFE phase. The white solid lines denote regions showing an evident AFD_y order. The oxygen displacements range from about -18 to 18 pm along both directions.

boundary of the AFE phase (left side) with the intermediate phase (right side) (**Figure 2a**). Referring to the oxygen atoms locating at the neutral sites (red solid lines), horizontal chains of oxygen atoms displacing along the γ direction clearly manifest the AFD order of the AFE phase. While in the intermediate phase, the oxygen atoms originally locating at the neutral sites also exhibit buckling behaviors on every other row. Analogously, vertical chains of oxygen atoms displacing along the x direction also show distinct behaviors between these two phases. Nevertheless, the characteristic antiparallel Pb displacements are maintained throughout the entire region and their unit-cell sizes appear to be the same.

Specifically, the displacement behaviors of oxygen are indexed by symbols of +, -, and 0 along the orthogonal $x/[100]_{O}$ and $y/[010]_{O}$ directions. Along the y direction, it is seen that the displacement sequences are changed from (+, 0, -, 0)and (-, 0, +, 0) in the AFE phase to (+, 0, -, +) and (-, 0, +, -)in the intermediate phase, which give rise to the FD_v component. At the orthorhombic unit-cell scale, the net displacement of oxygen is separately created along the odd- and even-column (Oo and Oe) atoms, but the alternation in direction cancels each other out (y-direction black arrows in Figure 2a). Along the x direction, the alteration of (-, 0, +, 0) in the AFE phase to (-, 0, +, +) in the intermediate phase results in an overall net displacement of oxygen atoms, which gives rise to the FD_r component. This indicates a clear AFD-FD transition of oxygen octahedra during the phase transition and a net polarization is expected to develop along this direction in the intermediate phase.

Based on the 2D Gaussian fitting to intensity peaks of oxygen columns, the displacement behavior of oxygen in image #7 is calculated and mapped over an area of $\approx 9 \times 9$ nm² (Figure S1, Supporting information). Along the x direction, it is seen that the FD $_x$ component prevails but mixes with the AFD $_x$ component (Figure 2b). Meanwhile, a reversal of net oxygen displacement seems to occur in the upper-right corner region

without destroying the antiparallel Pb order. Along the y direction, a complex texturing of the FD $_y$ with the AFD $_y$ component is also discernible from regions marked by white solid lines (Figure 2c). Comparison of the x- and y-component maps suggests that the AFD $_x$ -FD $_x$ transition initiates the AFE–FE phase transition. Furthermore, it is noticed that the net displacements of oxygen may also occur along the y direction inside the intermediate phase (Figure S2, Supporting information).

To quantify structural details of the intermediate phase, iterative image simulations associated with comparison to the experimental image were performed on a local region of image #7 with a uniform FD_x and FD_y distribution (**Figure 3a**,b). Relative to the centrosymmetric atomic sites in the cubic phase (see the Experimental Section), the atomic displacements in the experimental image are extracted by averaging along x and plotted along the y direction, and are taken as targets for the image simulation. It is seen that the antiparallel displacement of Pb atoms, with a magnitude of ≈ 25 pm, is well retained along the x direction, and the small displacement along the y direction is well within the measurement error (Figure 3c,d). With reservation of antiparallel Zr displacement in pairs along the x direction, the displacement along the y direction is increased from 1 to ≈ 8 pm (Figure 3e,f).

Pertinent to the AFE–FE transition, the critical atomic displacements occur to the oxygen atoms. Compared with the AFD $_x$ component, every other two rows of oxygen atoms, originally locating at the neutral positions, clearly displace toward the positive the x direction, e.g., the Oe-x atoms (Figure 3g). This leads to doubling of the AFE orthorhombic unit cell along the $b_{\rm O}$ axis, i.e., the lattice parameters of the FD phase are $b_{\rm O}' = 2b_{\rm O}$ and $a_{\rm O}' = a_{\rm O}$ (assuming $c_{\rm O}' = c_{\rm O}$) (Figure S3, Supporting information). For displacements along the y direction, every-other-row oxygen atoms, originally locating at the neutral sites, displace toward the negative direction, which maintains the lattice periodicity of the AFE phase. The Oo atoms show a similar behavior to that of Oe atoms along the x direction, but

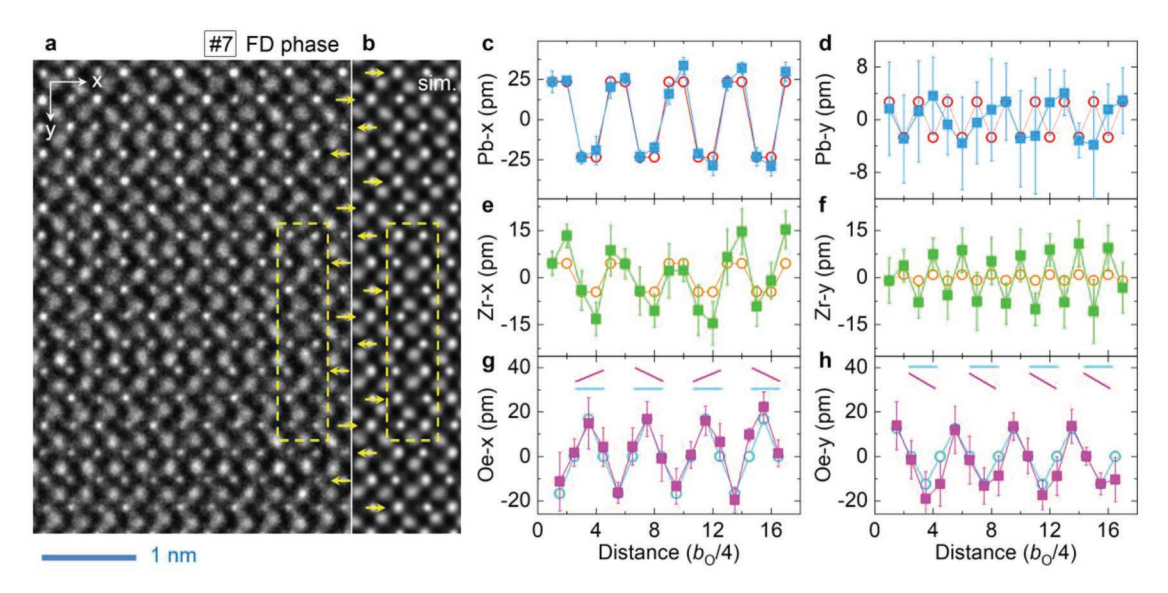


Figure 3. a,b) Atomic-resolution experimental (#7) and simulated (thickness = 9.9 nm; defocus = 8.0 nm) image of the FE–FD phase viewed along the [001]_O direction. The yellow arrows and dashed rectangles mark the antiparallel Pb displacements and the unit cell, respectively. c–h) Atomic displacements of Pb, Zr, and Oe (even-column oxygen) of the FE–FD phase, plotted as a function of distance along the y direction (solid squares), and compared with that of the AFE–AFD phase (empty circles), respectively. The Oo (odd-column oxygen) displacement is presented in Figure S4 of the Supporting Information. The pink solid lines in (g,h) highlight the FD oxygen displacements against the originally centrosymmetric positions (cyan solid lines).

the atoms responsible for the FD order exhibit an opposite displacement feature along the *y* direction (Figure S4, Supporting information).

With respect to the AFE–AFD phase, an ideal unit cell of the FD phase is illustrated along the $[001]_{\rm O}$ direction, where the FD oxygen displacements are highlighted by blue arrows (**Figure 4**a). In terms of the displacements of Pb, Zr, and O atoms, the spontaneous polarization ($P_{\rm S}$) of the FD phase is calculated along the x and y directions based on a sliding unit

cell.^[15] It is seen that both $P_{\rm SX}$ and $P_{\rm SY}$ exhibit sinusoidal wave profiles and their mean values are $\langle P_{\rm SX} \rangle = -2.8~\mu {\rm C~cm^{-2}}$ and $\langle P_{\rm SY} \rangle \approx 0$ (Figure 4b and Experimental Section). This demonstrates that breaking of spatial inversion symmetry by the AFD–FD transition allows emergence of $P_{\rm S}$ in the intermediate phase. Specifically, it is found that tails of the 2D polarization vectors, composed of the fitted sinusoidal profiles, can be nicely approximated by a curtate cycloid, which has a periodicity of $4b_{\rm O}$ along the γ direction (Figure 4c; Figure S5, Supporting

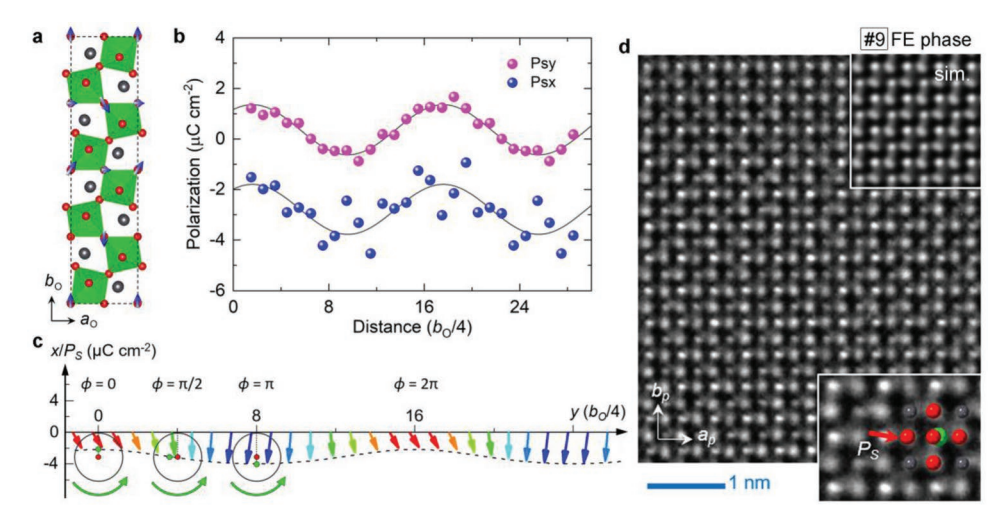


Figure 4. a) Illustration of an ideal unit cell of the FE–FD phase by properly adjusting positions of certain oxygen atoms (blue arrows) in the AFE–AFD phase. b) Calculated (solid symbols) and sinusoidal-wave-fitted (solid lines) polarization profiles from the atomic positions shown in Figure 3c–h. c) 2D plot of polarization vectors based on the wavy profile fitting. Their tails are nicely approximated by a curtate cycloid (black dashed line) and several phases ($\phi = 0$, $\pi/2$, and π) of the fixed point (green circles) on the radius of the rolling circle is marked out (see more details in Figure S5 in the Supporting Information). d) Atomic-resolution image (#9) of the FE_M phase recorded along the [001]_p direction. The insets are the simulated image (thickness = 9.6 nm; defocus = 8.8 nm) and a magnified area with overlapping of the structure model. Pb: black; Zr: green; O: oxygen.

Information). When structural defects appear, e.g., the translational boundaries,^[35,36] the commensurate relation of polarization with lattice will be broken in periodicity.

With further electron-beam irradiation, the FE-FD phase transforms completely into the FE pseudocubic phase, in which the oxygen octahedra are free of tilting or rotation (Figure 4d). The atomically resolved TEM image (#9) shows that both O-Zr/O-O and O-Pb-O columns form zigzag chains along the $b_{\rm p}$ axis. Based on the available imaging conditions, our quantitative image simulation reveals that the FE phase adopts a monoclinic symmetry. Referring to center of the unit cell, the Zr atom and oxygen octahedron displace opposite to each other by 7.9 and -12.1 pm along the a_p direction. Meanwhile, the Zr atom shift by ≈7 pm from the oxygen octahedral center along the b_n direction. Different from the monoclinic PbZr_{1-x}Ti_xO₃ $(x \approx 0.5)$, [23] the monoclinic PbZrO₃ resembles the rhombohedral $BaTiO_3^{[37]}$ in structure and has a polarization of P_{SX} = 31.1 μ C cm⁻² and $P_{SY} = 5.8 \mu$ C cm⁻² (Figure S6, Supporting information). The net polarization $P_S = 31.7 \mu C \text{ cm}^{-2}$ is about half of the FE_R phase (55 µC cm⁻²) of PbZrO₃ obtained by firstprinciples calculations.^[38] Its rotatable polarization orientation is illustrated in Figure S7 of the Supporting information.

In the ordinary FE phase zone (Figure 1c–e), we have observed the increase of lattice parameters and expansion of unit-cell volume at t > 60 s. The atomic-resolution TEM images (#13 and #14 in Figure S8 in the Supporting Information) indicate that this is ascribed to a first-order FE_M–FE_R phase transition.^[39] In the virgin FE state of PbZrO₃, the FE_R phase with a larger volume than the coexisting FE_M phase at nanoscale further supports the transition tendency (Figure S9, Supporting Information). These results therefore conclude a hierarchical evolution of cationic and oxygen octahedral polarity in PbZrO₃

(**Figure 5**a–d). It is noticed that the time-dependent change of volume and polarization, including emergence, enhancement and rotation of $P_{\rm S}$, [40] well corresponds to the macroscopic change of polarization and strain measured under application of electric field (Figure S10, Supporting information).

By combining the ground-state energy of different structural phases [41] with our experimental observations, it is interesting to note that the high-energy-state monoclinic phase appears prior to the low-energy-state rhombohedral phase (Figure 5e). Nevertheless, such a phase-transition route nicely follows a monotonic increase of the polarization, where the $P_{\rm S}$ ranges from \approx 38 to 55 μ C cm⁻² for the FE_R phase. [38,42] This implies that the energy is stored in a very complicated manner. Referring to the AFE orthorhombic phase, the 0.04–0.21 eV energy gap with the FE_M and FE_R phase indicates that about 10–57 J cm⁻³ is stored during the phase transition, which well agrees with the first-principles calculated value of \approx 19 J cm⁻³ at 900 kV cm⁻¹ in PbZrO₃. [4]

Clearly, the transfer and storage of electron-beam energy is realized through the complex electron–specimen interactions and the excited phase transitions. [29] Regarding the driving force for the dynamic transition, the following experimental facts indicate that this is governed by the charging effect, rather than the heating effect. i) As frequently seen in our experiments, the charging effect leads to a random motion of the specimen. As a function of irradiation time, the unit-cell volume of AFE PbZrO₃ continuously decreases (Figure S11, Supporting Information). This is opposite to the heating effect that leads to expansion of the unit-cell volume. [43] ii) On being heated to $\approx T_{\rm C}$, the characteristic Pb displacements along [100]_O direction are reduced to ≈ 17 pm. However, such a reduction in magnitude was not observed in the AFE–AFD and FE–FD phase of

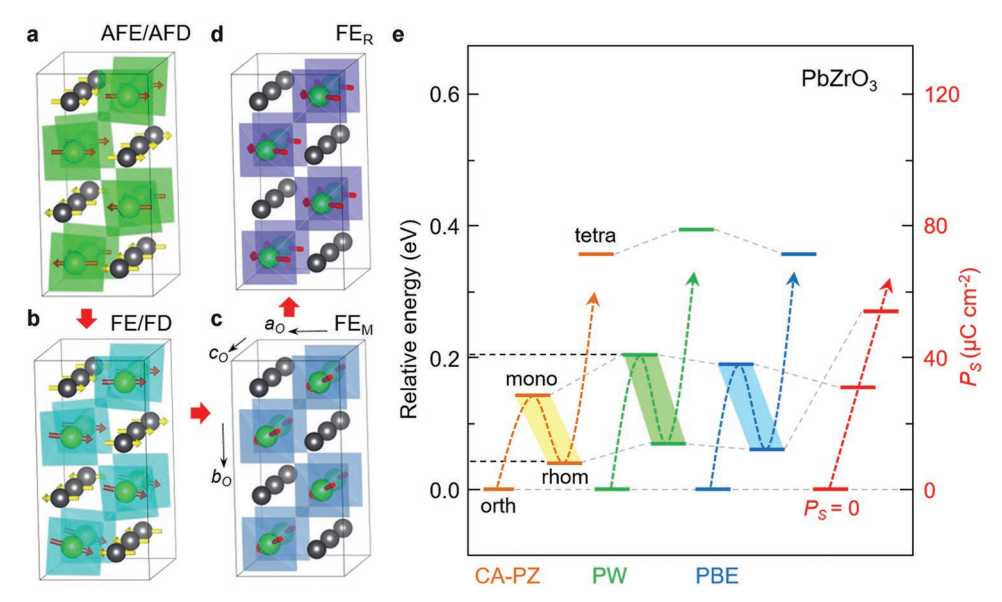


Figure 5. a–d) Hierarchical evolution of cationic (yellow arrows) and oxygen-octahedral (red arrows) polarity during the phase transitions in an orthorhombic framework. The polarization is running around $[\overline{1}00]_O$, along $[1\nu\overline{1}]_O$ (or $[1\nu\overline{1}]_O$ with 0.25 < ν < 0.5) and $[20\overline{1}]_O$ (or $[201]_O$) direction in the FE/FD, FE_M, and FE_R phases, respectively. e) Ground-state energy of the orthorhombic (ortho), monoclinic (mono), rhombohedral (rhom), and tetragonal (tetra) phases calculated by using different functionals, [41] i.e., the Ceperley–Alder–Perdew–Zunger (CA-PZ), Perdew–Wang (PW), and Perdew–Burke–Ernzerhoff (PBE), respectively. The phase-transition pathway (orange, green, and blue) and the monotonic increase of polarization (red) are denoted by dashed lines with arrows.



www.advancedsciencenews.com

ADVANCED MATERIALS

www.advmat.de

PbZrO₃. In addition, a reversed evolution sequence indicates that the AFE phase of PbZrO₃ stems from a "commensurate" FE–FD phase, rather than an "incommensurate" phase. [44] This is also supported by observation of modulated phases near the FE–AFE phase boundary in Sm-doped BiFeO₃. [45]

In summary, our time- and atomic-resolution quantitative electron microscopy study provides an unprecedented insight to comprehend the AFE–FE phase transitions in energy-storage PbZrO₃ and derived compounds.^[14] More intriguingly, our results establish an unconventional FE category—the FD phase, which is characteristic of a cycloidal polarization order and is distinct from the ordinary FEs and ZnSnO₃-like oxides.^[46,47] Analogous to various noncollinear spin structures in magnets,^[48] a noncollinear polarization order was reported for the first time in the unconventional FE materials. Our findings offer a plethora of opportunities to explore novel polarization orders in many different kinds of dielectric materials.^[49] It is also believed that our results may boost the study of energy-storage nonpolar materials at multiple scales in the future.

Experimental Section

Sample Preparation: The PbZrO $_3$ single crystals were grown by flux method with the PbO–B $_2$ O $_3$ mixture (soaking at 1050 K) used as a solvent. Details about the cooling procedures and removal of the residuals were presented elsewhere. $^{[15]}$ The lamella specimens were prepared using an FEI Helios Nanolab 400s focused ion beam system. To remove the contamination and the damaged layers, plasma cleaning and NanoMill Model 1040 system operated at 500 V were used to clean and mill the lamella samples. The lamella samples were heated above $T_{\rm C}$ and then cooled at ≈ 9 K min $^{-1}$ to recover the AFE orthorhombic phase from the FE phase at the thin edges. $^{[50,51]}$

Electron Microscopy Imaging Experiments: The diffraction contrast analysis and SAED experiments were carried out on an FEI Tecnai F20 microscope. The atomic resolution TEM study was performed on an FEI Titan 80–300 microscope, which is equipped with a Cs corrector for the objective lens and is operated at an accelerating voltage of 300 kV. The available point resolution was better than 80 pm and a dose rate of the electron beam was $\approx 1.3 \times 10^6$ e nm $^{-2}$ s $^{-1}$. A 2k \times 2k Gatan UltraScan 1000 CCD camera was used for the image acquisition and each frame exposure time was 0.8 s. It is noted that the energy transferred from the electron beam to the atom is inversely proportional to the atomic number. [52] After the 60 s irradiation, the lattice parameters were found to increase again with time. Apart from the FEM–FER transition, oxygen vacancies were also found in some local areas of the atomic-resolution images.

Image and Polarization Quantification: After filtering the image in a proper way, [32] quantitative measurements of atomic column positions were carried out by fitting the column intensities with 2D Gaussian peaks on the basis of maximum likelihood estimation. [53] Structure modeling, high-resolution image simulation and SAED simulation were carried out using CrystalKit-MacTempas software package. The imaging parameters used in image simulation are $C_S = -12 \, \mu m$, $A1 = 2.5 \, nm$, $A2 = 30 \, nm$, and $B2 = 30 \, nm$. With the structural models that lead to the best matching of the simulated images with the experimental ones, the polarization is calculated in terms of the formula $P_S = \frac{1}{V} \sum \delta_i Z_i^a$, where δ_i is atomic displacement with respect to the ideal position in the cubic phase and Z_i^a is the effective charge for the element. The Born charges [41] are $Z^*_{Pb} = 3.56$, $Z^*_{Zr} = 4.91$, and $Z^*_{O} = -2.82$ for the FD phase and $Z^*_{Pb} = 3.73$, $Z^*_{Zr} = 4.71$, and $Z^*_{O} = -2.81$ for the monoclinic phase.

Definition of Lattice Coordinate Origin: Considering the fact that most atomic columns in the FE-FD phase have displacements with respect to their ideal positions in the cubic phase, it is not wise to measure the relative displacements between different column types

from the experimental image. Since the antiparallel Pb atoms, with equal magnitudes, undergo the identical shift behaviors in the AFD and FD phases (Figure 2a), the centrosymmetric lattice origin is defined as follows: 1) With the calculated mean lattice parameter, $a_{\rm O}$, the displacements of Pb along the [100]_O direction is averaged with respect to the image coordinate origin. 2) The obtained Pb-displacement profile is linearly fitted and subtracted to fulfill the equal but opposite Pb displacements with respect to their ideal positions in the cubic phase. The linear background is taken as a reference for quantifying the net displacements of Zr and oxygen columns from the experimental image. Similar method is applied to quantify the atom-column displacements along the [010]_O direction. For the FE monoclinic phase (image #9), the relative atom-column displacements are calculated by taking the Pb and oxygen columns as references. [53]

Supporting Information

Supporting Information is available from the Wiley Online Library or from the author.

Acknowledgements

The research leading to these results has received funding from the European Research Council under the EU 7th Framework Programme (FP7/2007-2013)/ERC Grant Agreement No. [268058] Mobile-W. This work was supported by the National Science Centre, Poland, within the project 2016/21/B/ST3/02242. The authors thank D. Meertens for sample preparation using the focused ion beam system.

Conflict of Interest

The authors declare no conflict of interest.

Author Controbutions

X.-K.W. conceived the idea and wrote the manuscript. X.-K.W. conducted the experiments, image simulation, and data analysis with support from C.-L.J., J.M., and R.E.D.B. H.-C.D. provides support in data measurement and analysis. K.R. characterized the optical property of the PbZrO3 single-crystal samples.

Keywords

cycloidal polarization, energy storage, ferrodistortive phase, $PbZrO_3$, phase transition

Received: November 2, 2019 Revised: December 15, 2019 Published online: January 24, 2020

B. Chu, X. Zhou, K. Ren, B. Neese, M. Lin, Q. Wang, F. Bauer, Q. M. Zhang, *Science* 2006, 313, 334.

^[2] Q. Li, L. Chen, M. R. Gadinski, S. Zhang, G. Zhang, U. Li, E. lagodkine, A. Haque, L. Q. Chen, N. Jackson, Q. Wang, *Nature* 2015, 523, 576.

^[3] H. Pan, F. Li, Y. Liu, Q. W. Zhang, Meng, S. Lan, Y. Zheng, J. Ma, L. Gu, Y. Shen, P. Yu, S. Zhang, L.-Q. Chen, Y.-H. Lin, C.-W. Nan, Science 2019, 365, 578.

- [29] V. I. Arkhipox, A. I. Rudenko, G. M. Sessier, J. Phys. D: Appl. Phys. 1993, 26, 1298
- [30] R. F. Egerton, P. Li, M. Malac, Micron 2004, 35, 399.
- [31] L. Yao, S. Majumdar, L. Akaslompolo, S. Inkinen, Q. H. Qin, S. van Dijken, Adv. Mater. 2014, 26, 2789.
- [32] C.-L. Jia, S.-B. Mi, K. Urban, I. Vrejoiu, M. Alexe, D. Hesse, Nat. Mater. 2007, 7, 57.
- [33] C. L. Jia, L. Houben, A. Thust, J. Barthel, *Ultramicroscopy* **2010**, *110*, 500.
- [34] K. Yamasaki, Y. Soejimaa, K. F. Fischer, Acta Crystallogr. 1998, 54, 524
- [35] X.-K. Wei, C.-L. Jia, K. Roleder, N. Setter, *Mater. Res. Bull.* **2015**, *62*, 101.
- [36] X.-K. Wei, K. Vaideeswaran, C. S. Sandu, C.-L. Jia, N. Setter, Adv. Mater. Interfaces 2015, 2, 1500349.
- [37] G. H. Kwei, A. C. Lawson, S. J. L. Billinge, S. W. Cheong, J. Phys. Chem. 1993, 97, 2368.
- [38] R. Kagimura, D. Singh, Phys. Rev. B 2008, 77, 104113.
- [39] D. Vanderbilt, M. Cohen, Phys. Rev. B 2001, 63, 094108.
- [40] H. Fu, R. E. Cohen, Nature 2000, 403, 281.
- [41] J. A. Rodriguez, A. Etxeberria, L. González, A. Maiti, J. Chem. Phys. 2002, 117, 2699.
- [42] M. Avdeev, J. D. Jorgensen, S. Short, G. A. Samara, E. L. Venturini, P. Yang, B. Morosin, *Phys. Rev. B* **2006**, *73*, 064105.
- [43] R. W. Whatmore, A. M. Glazer, J. Phys. C: Solid State Phys. 1979, 12, 1505.
- [44] A. K. Tagantsev, K. Vaideeswaran, S. B. Vakhrushev, A. V. Filimonov, R. G. Burkovsky, A. Shaganov, D. Andronikova, A. I. Rudskoy, A. Q. Baron, H. Uchiyama, D. Chernyshov, A. Bosak, Z. Ujma, K. Roleder, A. Majchrowski, J. H. Ko, N. Setter, *Nat. Commun.* 2013, 4, 2229.
- [45] A. Y. Borisevich, E. A. Eliseev, A. N. Morozovska, C. J. Cheng, J. Y. Lin, Y. H. Chu, D. Kan, I. Takeuchi, V. Nagarajan, S. V. Kalinin, Nat. Commun. 2012, 3, 775.
- [46] J. Y. Son, G. Lee, M.-H. Jo, H. Kim, H. M. Jang, Y.-H. Shin, J. Am. Chem. Soc. 2009, 131, 8386.
- [47] T. Gu, T. Scarbrough, Y. Yang, J. Iniguez, L. Bellaiche, H. J. Xiang, Phys. Rev. Lett. 2018, 120, 197602.
- [48] S. W. Cheong, M. Mostovoy, Nat. Mater. 2007, 6, 13.
- [49] J. M. Rondinelli, C. J. Fennie, Adv. Mater. 2012, 24, 1961.
- [50] E. A. Eliseev, M. D. Glinchuk, Phys. B 2007, 400, 106.
- [51] K. Roleder, J. Dec, J. Phys.: Condens. Matter 1989, 1, 1503.
- [52] D. B. Williams, C. B. Carter, Transmission Electron Microscopy: A Textbook for Materials Science, Plenum, New York 1996.
- [53] X.-K. Wei, Y. Yang, L. J. McGilly, L. Feigl, R. E. Dunin-Borkowski, C.-L. Jia, L. Bellaiche, N. Setter, *Phys. Rev. B* 2018, 98, 020102 (R).

- [4] B. Xu, J. Iniguez, L. Bellaiche, Nat. Commun. 2017, 8, 15682.
- [5] Q. Fan, C. Ma, Y. Li, Z. Liang, S. Cheng, M. Guo, Y. Dai, C. Ma, L. Lu, W. Wang, L. Wang, X. Lou, M. Liu, H. Wang, C.-L. Jia, *Nano Energy* 2019, 62, 725.
- [6] B. Peng, Q. Zhang, X. Li, T. Sun, H. Fan, S. Ke, M. Ye, Y. Wang, W. Lu, H. Niu, J. F. Scott, X. Zeng, H. Huang, Adv. Electron. Mater. 2015, 1, 1500052.
- [7] H. Pan, J. Ma, J. Ma, Q. Zhang, X. Liu, B. Guan, L. Gu, X. Zhang, Y. J. Zhang, L. Li, Y. Shen, Y. H. Lin, C. W. Nan, *Nat. Commun.* 2018, 9, 1813.
- [8] H. Wang, Y. Liu, T. Yang, S. Zhang, Adv. Funct. Mater. 2019, 29, 1807321.
- [9] I. MacLaren, R. Villaurrutia, B. Schaffer, L. Houben, A. Peláiz-Barranco, Adv. Funct. Mater. 2012. 22. 261.
- [10] O. E. Fesenko, R. V. Kolesova, Y. G. Sindeyev, Ferroelectrics 1978, 20, 177.
- [11] C. T. Blue, J. C. Hicks, S. E. Park, S. Yoshikawa, L. E. Cross, Appl. Phys. Lett. 1996, 68, 2942.
- [12] Y. Cai, F. Phillipp, A. Zimmermann, L. Zhou, F. Aldinger, M. Rühle, Acta Mater. 2003, 51, 6429.
- [13] H. He, X. Tan, Phys. Rev. B 2005, 72, 024102.
- [14] L. Shebanov, M. Kusnetsov, A. Sternberg, J. Appl. Phys. 1994, 76, 4301.
- [15] X. K. Wei, A. K. Tagantsev, A. Kvasov, K. Roleder, C. L. Jia, N. Setter, Nat. Commun. 2014, 5, 3031.
- [16] X. Tan, C. Ma, J. Frederick, S. Beckman, K. G. Webber, D. J. Green, J. Am. Ceram. Soc. 2011, 94, 4091.
- [17] G. Shirane, E. Sawaguchi, Y. Takagi, Phys. Rev. 1951, 84, 476.
- [18] V. J. Tennery, J. Am. Ceram. Soc. 1966, 49, 483.
- [19] A. Roy Chaudhuri, M. Arredondo, A. Hähnel, A. Morelli, M. Becker, M. Alexe, I. Vrejoiu, Phys. Rev. B 2011, 84, 054112.
- [20] B. A. Scott, G. Burns, J. Am. Ceram. Soc. 1972, 55, 331.
- [21] E. Sawaguchi, J. Phys. Soc. Jpn. 1953, 8, 615.
- [22] G. Shirane, S. Hoshino, Acta Cryst. 1954, 7, 203.
- [23] B. Noheda, D. E. Cox, G. Shirane, J. A. Gonzalo, L. E. Cross, S. E. Park, Appl. Phys. Lett. 1999, 74, 2059.
- [24] H. Yokota, N. Zhang, A. Taylor, P. Thomas, A. Glazer, Phys. Rev. B 2009, 80, 104109.
- [25] X.-K. Wei, C.-L. Jia, T. Sluka, B.-X. Wang, Z.-G. Ye, N. Setter, Nat. Commun. 2016, 7, 12385.
- [26] A. Bussmann-Holder, J. H. Ko, A. Majchrowski, M. Gorny, K. Roleder, J. Phys.: Condens. Matter 2013, 25, 212202.
- [27] S. Aoyagi, Y. Kuroiwa, A. Sawada, H. Tanaka, J. Harada, E. Nishibori, M. Takata, M. Sakata, J. Phys. Soc. Jpn. 2002, 71, 2353.
- [28] Y. Kuroiwa, Y. Terado, C. Moriyoshi, Ferroelectrics 2007, 354, 158.